Combustion and Flame 160 (2013) 1594–1608

Contents lists available at SciVerse ScienceDirect

Combustion and Flame

journal homepage: www.elsevier.com/locate/combustflame

Measurements of temperature and hydroxyl radical generation/decay in lean fuel–air mixtures excited by a repetitively pulsed nanosecond discharge

Zhiyao Yin [a,*], Aaron Montello [a], Campbell D. Carter [b], Walter R. Lempert [a], Igor V. Adamovich [a]

[a] Michael A. Chaszeyka Nonequilibrium Thermodynamics Laboratories, Department of Mechanical Engineering, The Ohio State University, Columbus, OH 43210, United States
[b] Air Force Research Laboratory, Wright-Patterson AFB, OH 45433, United States

ARTICLE INFO

Article history:
Received 9 December 2012
Received in revised form 3 March 2013
Accepted 12 March 2013
Available online 10 April 2013

Keywords:
Plasma assisted combustion
Nanosecond pulse discharge
Low temperature plasmas
Laser Induced Fluorescence
Kinetic modeling

ABSTRACT

OH Laser Induced Fluorescence (LIF) and picosecond (ps), broadband Coherent Anti-Stokes Raman Spectroscopy (CARS) are used for time-resolved temperature and time-resolved, absolute OH number density measurements in lean H_2-air, CH_4-air, C_2H_4-air, and C_3H_8-air mixtures in a nanosecond (ns) pulse discharge cell/plasma flow reactor. The premixed fuel–air flow in the reactor, initially at $T_0 = 500$ K and $P = 100$ torr, is excited by a repetitive ns pulse discharge in a plane-to-plane geometry (peak voltage 28 kV, discharge gap 10 mm, estimated pulse energy 1.25 mJ/pulse), operated in burst mode at 10 kHz pulse repetition rate. In most measurements, burst duration is limited to 50 pulses, to preclude plasma-assisted ignition. The discharge uniformity in air and fuel–air flows is verified using sub-ns-gated images (employing an intensified charge-coupled device camera). Temperatures measured at the end of the discharge burst are in the range of $T = 550$–600 K, using both OH LIF and CARS, and remain essentially unchanged for up to 10 ms after the burst. Time-resolved temperature measured by CARS during plasma-assisted ignition of H_2-air is in good agreement with kinetic model predictions. Based on CARS measurement, vibrational nonequilibrium is not a significant factor at the present conditions.

Time-resolved, absolute OH number density, measured after the discharge burst, demonstrates that OH concentration in C_2H_4-air, C_3H_8-air, and CH_4 is highest in lean mixtures. In H_2-air, OH concentration is nearly independent of the equivalence ratio. In C_2H_4-air and C_3H_8-air, unlike in CH_4-air and in H_2-air, transient OH-concentration overshoot after the discharge is detected. In C_2H_4-air and C_3H_8-air, OH decays after the discharge on the time scale of ~0.02–0.1 ms, suggesting little accumulation during the burst of pulses repeated at 10 kHz. In CH_4-air and H_2-air, OH concentration decays within ~0.1–1.0 ms and 0.5–1.0 ms, respectively, showing that it may accumulate during the burst.

The experimental results are compared with kinetic modeling calculations using plasma/fuel chemistry model employing several H_2-air and hydrocarbon-air chemistry mechanisms. Kinetic mechanisms for H_2-air, CH_4-air, and C_2H_4-air developed by A. Konnov provide the best overall agreement with OH measurements. In C_3H_8-air, none of the hydrocarbon chemistry mechanisms agrees well with the data. The results show the need for development of an accurate, predictive low-temperature plasma chemistry/fuel chemistry kinetic model applicable to fuels C_3 and higher.

1. Introduction

Nonequilibrium plasmas formed by nanosecond (ns) duration pulsed discharges have shown significant effect on ignition delay reduction and flame stabilization [1–9]. The peak *reduced* electric field, defined as the ratio of electric field and total gas number density, (E/N), in these discharges is of the order of 10^2–10^3 Td (1 Td = 10^{-17} V cm^2), which enhances electronic excitation and dissociation of gas molecules, resulting in efficient generation of radical species. The radicals readily react with the fuel and oxidizer molecules, resulting in chain branching reactions and heat generation, which can eventually lead to ignition. To analyze quantitatively the impact of radicals produced in the plasma on fuel oxidation and ignition, time-resolved measurements of gas temperature and radical concentrations are required. Recently, laser diagnostics has been applied to quantitative analysis of plasma assisted ignition/combustion, such as OH Planar Laser Induced Fluorescence (PLIF) [10,11], saturated OH LIF [12] and O atom Two-photon Absorption LIF (TALIF) [13,14]. In our previous work, various laser diagnostics methods have been used for temporally

* Corresponding author. Address: W090 Scott Lab., 201. W 19th Ave., Columbus, OH 43210, United States.
E-mail address: yin.67@osu.edu (Z. Yin).

0010-2180/$ - see front matter © 2013 The Combustion Institute. Published by Elsevier Inc. All rights reserved.
http://dx.doi.org/10.1016/j.combustflame.2013.03.015

Report Documentation Page

Form Approved
OMB No. 0704-0188

1. REPORT DATE	2. REPORT TYPE	3. DATES COVERED
APR 2013		**00-00-2013 to 00-00-2013**

4. TITLE AND SUBTITLE	5a. CONTRACT NUMBER
Measurements of temperature and hydroxyl radical generation/decay in lean fuel-air mixtures excited by a repetitively pulsed nanosecond discharge	5b. GRANT NUMBER
	5c. PROGRAM ELEMENT NUMBER
6. AUTHOR(S)	5d. PROJECT NUMBER
	5e. TASK NUMBER
	5f. WORK UNIT NUMBER
7. PERFORMING ORGANIZATION NAME(S) AND ADDRESS(ES) **Ohio State University,Department of Mechanical Engineering,Michael A. Chaszeyka Nonequilibrium Thermodynamics Laboratories,Columbus,OH,43210**	8. PERFORMING ORGANIZATION REPORT NUMBER
9. SPONSORING/MONITORING AGENCY NAME(S) AND ADDRESS(ES)	10. SPONSOR/MONITOR'S ACRONYM(S)
	11. SPONSOR/MONITOR'S REPORT NUMBER(S)

12. DISTRIBUTION/AVAILABILITY STATEMENT
Approved for public release; distribution unlimited

13. SUPPLEMENTARY NOTES

14. ABSTRACT

OH Laser Induced Fluorescence (LIF) and picosecond (ps), broadband Coherent Anti-Stokes Raman Spectroscopy (CARS) are used for time-resolved temperature and time-resolved, absolute OH number density measurements in lean H2-air, CH4-air, C2H4-air, and C3H8-air mixtures in a nanosecond (ns) pulse discharge cell/plasma flow reactor. The premixed fuel?air flow in the reactor, initially at T0 = 500 K and P = 100 torr, is excited by a repetitive ns pulse discharge in a plane-to-plane geometry (peak voltage 28 kV, discharge gap 10 mm, estimated pulse energy 1.25 mJ/pulse), operated in burst mode at 10 kHz pulse repetition rate. In most measurements, burst duration is limited to 50 pulses, to preclude plasma-assisted ignition. The discharge uniformity in air and fuel?air flows is verified using sub-ns-gated images (employing an intensified charge-coupled device camera). Temperatures measured at the end of the discharge burst are in the range of T = 550?600 K, using both OH LIF and CARS, and remain essentially unchanged for up to 10 ms after the burst. Time-resolved temperature measured by CARS during plasmaassisted ignition of H2-air is in good agreement with kinetic model predictions. Based on CARS measurement vibrational nonequilibrium is not a significant factor at the present conditions.

Time-resolved, absolute OH number density, measured after the discharge burst, demonstrates that OH concentration in C2H4-air, C3H8-air, and CH4 is highest in lean mixtures. In H2-air, OH concentration is nearly independent of the equivalence ratio. In C2H4-air and C3H8-air, unlike in CH4-air and in H2-air transient OH-concentration overshoot after the discharge is detected. In C2H4-air and C3H8-air, OH decays after the discharge on the time scale of 0.02?0.1 ms, suggesting little accumulation during the burst of pulses repeated at 10 kHz. In CH4-air and H2-air, OH concentration decays within 0.1?1.0 ms and 0.5? 1.0 ms, respectively, showing that it may accumulate during the burst. The experimental results are compared with kinetic modeling calculations using plasma/fuel chemistry model employing several H2-air and hydrocarbon-air chemistry mechanisms. Kinetic mechanisms for H2- air, CH4-air, and C2H4-air developed by A. Konnov provide the best overall agreement with OH measurements. In C3H8-air, none of the hydrocarbon chemistry mechanisms agrees well with the data. The results show the need for development of an accurate, predictive low-temperature plasma chemistry/fuel chemistry kinetic model applicable to fuels C3 and higher.

15. SUBJECT TERMS

16. SECURITY CLASSIFICATION OF:			17. LIMITATION OF ABSTRACT	18. NUMBER OF PAGES	19a. NAME OF RESPONSIBLE PERSON
a. REPORT	b. ABSTRACT	c. THIS PAGE			
unclassified	**unclassified**	**unclassified**	**Same as Report (SAR)**	**15**	

and spatially resolved measurements in ns discharges in fuel–air mixtures, including absolute NO, OH, and O atom concentrations by LIF [15–18], rotational and N_2 vibrational temperatures by Coherent Anti-Stokes Raman Spectroscopy (CARS) [19–21], and rotational temperature by OH LIF [18].

In our previous measurements of ignition delay and OH concentration in H_2-air mixtures, two discharge operation regimes have been used. In the first approach, a ns pulse discharge operating at a high pulse repetition rate was maintained through the ignition process [17,22]. Kinetic modeling of the plasma chemical ignition process demonstrated that in this case ignition time had a fairly weak dependence on the details of kinetic mechanism. This occurs due to continuous generation of radicals during the discharge, overlapping with ignition, which largely "masks" such dependence. In the second approach, the discharge burst was terminated shortly before the onset of ignition [18]. At these conditions, electronically excited molecules and atoms generated during the discharge decay rapidly, such that oxidation of fuel–air mixtures is controlled primarily by low-temperature reactions of species in their ground electronic states, with the pool of radicals (primarily H, O, and OH) generated during the discharge. Therefore, this approach uncouples plasma chemical reactions from "conventional" chemical reactions, making analysis of kinetics more straightforward. In this case, ignition of H_2-air mixtures, initially at $T_0 = 500$ K, occurred when the temperature at the end of the discharge burst exceeded a threshold of approximately $T_f \approx 700$ K, about 200 K lower than autoignition temperature predicted by kinetic modeling [22]. Based on ignition time, time-resolved temperature, and time-resolved absolute OH concentration measurements using OH LIF [17,18,22], insight into the effect of super-equilibrium concentrations of radical species generated in low-temperature H_2-air plasmas has been obtained.

However, quantitative study of plasma assisted ignition kinetics by a repetitive ns pulse discharge could not be easily extended to hydrocarbon fuels, due to nonuniform ignition caused even by moderate plasma nonuniformity [18,22]. In the present work, this problem is circumvented by reducing the number of pulses in the discharge burst, as well as the equivalence ratio. This is done to study the mechanism of radical generation (with OH being the primary focus) in mildly preheated fuel–air mixtures excited by a repetitively pulsed ns discharge, as well OH production and decay after the discharge, before ignition would occur. The objectives of the present work are: (i) to use both OH LIF thermometry and picosecond (ps) CARS for time-resolved rotational temperature measurements of fuel–air mixtures after a ns pulse discharge burst, and (ii) to measure absolute, time-resolved OH concentrations in H_2-air and hydrocarbon-air mixtures excited by the discharge after it is turned off. Thus, plasma chemical reactions and "conventional" chemical reactions are separated in time, similar to the approach used in our previous work [18,22]. These measurements are conducted for several different fuels, over a range of equivalence ratios. The results are compared with kinetic modeling calculations, to assess the applicability of H_2-air and hydrocarbon-air chemistry mechanisms at the present low-temperature conditions.

2. Experimental

The experimental setup used in the present work, shown schematically in Fig. 1, is similar to the one used in our previous studies [18]. The discharge cell/plasma flow reactor consists of a 280-mm-long, 22 mm × 10 mm rectangular inner cross section quartz channel with wall thickness of 1.75 mm. Two plane quartz windows, 1 mm thick each, are fused to the ends of the channel, providing optical access in the axial direction. A 60-mm-long, right-angle fused silica prism is placed along the channel to provide optical access from the side (see Fig. 1). The entire assembly is heated in a tube furnace (Thermcraft, Ltd., with 152-mm-diameter, 254-mm-long heated section), to improve plasma stability. A 1-m-long quartz tube coil inlet (see Fig. 1) preheats the fuel–air flow to the furnace temperature, which was verified by thermocouple measurements. Two 6-mm-diameter quartz-to-stainless-steel adaptors connect the reactor to the gas delivery system. Fuel and air flow rates through the reactor are metered by MKS mass flow control-

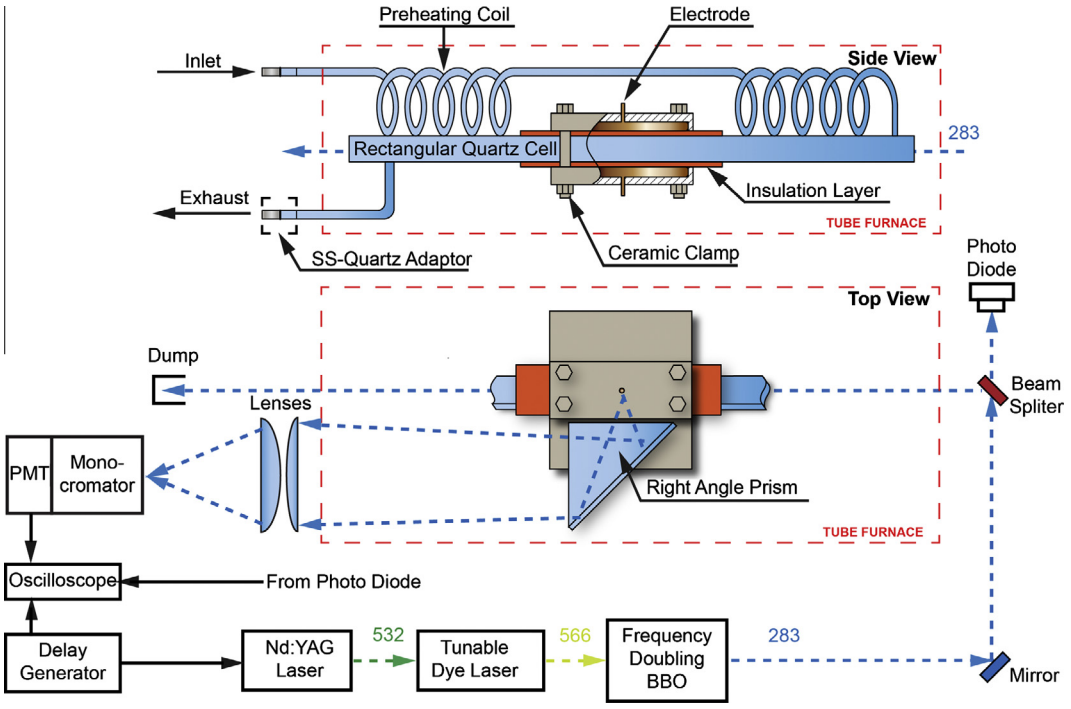

Fig. 1. Schematic diagram of the preheated plasma assisted ignition test cell and OH LIF apparatus.

lers (<0.4% error at the experimental flow rates, according to the manufacturer's specifications). Fuel and air flows are premixed before entering the cell.

Two 14 mm × 60 mm rectangular plate copper electrodes, rounded at the edges, are placed on the top and bottom of the quartz channel, as shown in Fig. 1, and held in place by ceramic clamps. A 1.6-mm-thick high-temperature perfluoroelastomer sheet (Kalrez, DuPont) is placed between each electrode and the channel wall, to reduce air gaps and prevent corona discharge outside the cell. Thus, the total distance between the electrodes is approximately 17 mm, with the discharge gap (distance between top and bottom quartz walls) of 10 mm. The electrodes are connected to an FID GmbH FPG 60-100MC4 pulse generator (peak voltage up to 30 kV, pulse duration of 5 ns, repetition rate up to 100 kHz). In the present work, the pulser is operated in repetitive burst mode, producing bursts of 50 pulses at a pulse repetition rate of 10 kHz and burst repetition rate of 5 Hz.

A schematic diagram of the OH LIF setup is also shown in Fig. 1. Briefly, the 532 nm output from an Nd:YAG laser (Continuum, Model Powerlite 8010) is used to pump a tunable dye laser (Laser Analytical Systems, Model LDL 20505), the output of which is frequency doubled by a β Barium Borate (BBO) crystal (wavelengths shown in Fig. 1 correspond to OH A–X (1,0) pumping). While the flash lamp of the Nd:YAG laser is operated at 10 Hz, *Q*-switching controlling the laser output is maintained at 5 Hz, to match the burst repetition rate of the pulser and to probe OH after each discharge burst. A delay generator is used to control the delay between the discharge burst and the laser pulse. A half wave plate and thin film polarizer pair is used to control the UV beam energy for LIF operation in the linear regime (below 5 μJ/pulse). The UV beam energy is monitored using a photodiode placed after a beam splitter (see Fig. 1).

OH concentration and rotational temperature (assumed to be in equilibrium with the translational temperature) are measured on the channel centerline by OH LIF in lean CH_4-, C_2H_4-, C_3H_8-, and H_2-air mixtures, each at four different equivalence ratios, at flow velocity through the reactor of $u \approx 40$ cm/s. The purity of the fuels is as follows: 99.0% for CH_4 (<0.02% of O_2, H_2O, and CO_2 combined, <0.2% of N_2), 99.5% for C_2H_4 and C_3H_8, and 99.999% for H_2. The compressed air cylinder used is Ultra Zero grade, with 19.5–23.5% of O_2 and <2 ppm H_2O. A low discharge burst repetition rate, 5 Hz, is chosen to keep the delay between the bursts longer than the residence time of the flow in the plasma, ~0.1 s, such that the flow in the reactor would experience only one burst. The low flow velocity also improves flow preheating in the inlet coil and reduces pressure drop across the reactor.

For relative OH concentration measurements, the $Q_1(3)$ line in the OH A–X (1,0) band is used to maximize signal-to-noise ratio at temperatures below 600 K. For OH thermometry, four additional lines in the (1,0) band system are used to generate a more accurate Boltzmann fit for rotational temperature, including the $P_1(1)$, $Q_1(2)$, $Q_1(4)$, and $Q_1(5)$ lines. The choice of the excitation lines, as well as LIF signal processing was discussed in detail in Ref. [17]. Additional details of LIF diagnostics are discussed in Section 4. LIF is collected from the center of the discharge, a region approximately 15-mm-long, via a right angle prism and fused silica lenses, and directed to a photomultiplier tube (PMT) (Hamamatsu, Model R106) in combination with a small monochromator (Horiba, Model H-10), which is used to collect fluorescence signal only from (0,0) and (1,1) transitions. The LIF signal is integrated over a 100-ns gate and analyzed in real time during the experiment using a programmable digital oscilloscope with 1-GHz bandwidth (LeCroy, Model WAVEPRO 7100A).

Relative OH LIF concentrations measured using (1,0) excitation are calibrated using the LIF signal from $R_1(4)$ excitation in the (0,0) band and Rayleigh scattering at the wavelength close to the center of the (0,0) fluorescence band, 308 nm, as discussed in detail in Section 4. For calibration using Rayleigh scattering, the flow channel/discharge cell has been modified to accommodate the entrance and exit windows set at Brewster's angle. Note that using Rayleigh scattering calibration requires no change in optical alignment, therefore mitigating uncertainties encountered with the use of an atmospheric-pressure Hencken burner flame [18].

Rotational temperature and vibrational temperature of N_2 on the centerline of the discharge cell/plasma flow reactor are also measured by ps Coherent Anti-Stokes Raman Spectroscopy (CARS) diagnostics described in detail in Ref. [21] and shown schematically in Fig. 2. Briefly, in this system a broadband Stokes beam is generated by an in-house fabricated modeless dye laser, with conversion efficiency of approximately 6%. The dye laser is pumped by an Ekspla SL-333 Nd:YAG laser, generating output pulses ~150 ps in duration, with energy output of up to 120 mJ/pulse at 532 nm. The Nd:YAG laser also generates the pump/probe beams for the CARS mixing. The dye laser output is centered near 604 nm, with a full width at half maximum of approximately 5–6 nm. In the present work, Unstable-resonator Spatially Enhanced Detection

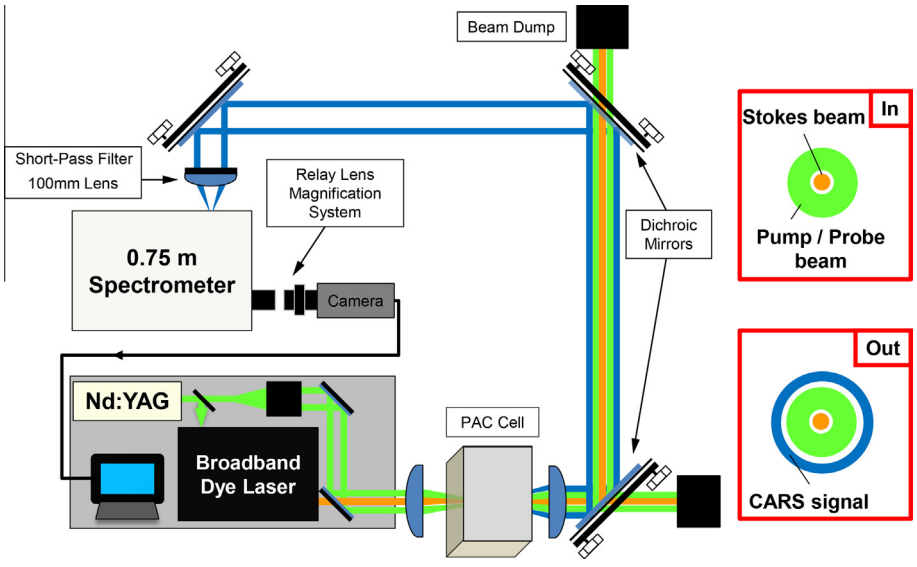

Fig. 2. Schematic diagram of ps USED-CARS apparatus.

Table 1
Dominant primary radical species generation processes in the plasma [12,15,18,21].

	Process	Rate (cm^3/s)
A1	$N_2 + e^- = N_2(A^3\Sigma, B^3\Pi, C^3\Pi, a'^1\Sigma) + e^-$	σ[a]
A2	$N_2 + e^- = N(^4S) + N(^4S) + e^-$	σ
A3	$O_2 + e^- = O(^3P) + O(^3P,^1D) + e^-$	σ
A4	$N_2(C^3\Pi) + O_2 = N_2(B^3\Pi) + O_2$	3.0×10^{-10}
A5	$N_2(a'^1\Sigma) + O_2 = N_2(B^3\Pi) + O_2$	2.8×10^{-11}
A6	$N_2(B^3\Pi) + O_2 = N_2(A^3\Sigma) + O_2$	3.0×10^{-10}
A7	$N_2(A^3\Sigma) + O_2 = N_2 + O + O$	2.5×10^{-12}
H1	$H_2 + e^- = H + H + e^-$	σ[2]
H2	$N_2(a'^1\Sigma) + H_2 = N_2 + H + H$	2.6×10^{-11}
H2	$N_2(B^3\Pi) + H_2 = N_2(A^3\Sigma) + H_2$	2.5×10^{-11}
H4	$N_2(A^3\Sigma) + H_2 = N_2 + H + H$	$4.4 \times 10^{-10}\exp(-3170/T)$
H5	$O(^1D) + H_2 = H + OH$	1.1×10^{-10}
M1	$CH_4 + e^- = CH_3 + H + e^-$	σ
M2	$N_2(A^3\Sigma) + CH_4 = N_2 + CH_3 + H$	$1.2 \times 10^{-10}\exp(-3500/T)$
M3	$N_2(B^3\Pi) + CH_4 = N_2 + CH_3 + H$	3.0×10^{-10}
M4	$N_2(C^3\Pi) + CH_4 = N_2 + CH_3 + H$	5.0×10^{-10}
M5	$N_2(a'^1\Sigma) + CH_4 = N_2 + CH_3 + H$	3.0×10^{-10}
E1	$C_2H_4 + e^- = \text{products}$[3] $+ e^-$	σ
E2	$N_2(A^3\Sigma) + C_2H_4 = N_2 + C_2H_3 + H$	9.7×10^{-11}
E3	$N_2(B^3\Pi) + C_2H_4 = N_2 + C_2H_3 + H$	3.0×10^{-10}
E4	$N_2(C^3\Pi) + C_2H_4 = N_2 + C_2H_3 + H$	3.0×10^{-10}
E5	$N_2(a'^1\Sigma) + C_2H_4 = N_2 + C_2H_3 + H$	4.0×10^{-10}
P1	$N_2(A^3\Sigma) + C_3H_8 = N_2 + C_3H_6 + H_2$	1.2×10^{-12}
P2	$N_2(B^3\Pi) + C_3H_8 = N_2 + C_3H_6 + H_2$	3.0×10^{-10}
P3	$N_2(C^3\Pi) + C_3H_8 = N_2 + C_3H_6 + H_2$	3.0×10^{-10}
P4	$N_2(a'^1\Sigma) + C_3H_8 = N_2 + C_3H_6 + H_2$	4.0×10^{-10}

[a] Calculated by the Boltzmann solver from the experimental cross sections.
[b] Sum of electronic excitation cross sections ($b^3\Sigma$, $b^1\Sigma$, $c^3\Pi$, $a^3\Sigma$, $c^1\Pi$, and $d^3\Pi$).
[c] Three dissociation channels into $C_2H_3 + H$, $C_2H_2 + H_2$, and $C_2H_2 + H + H$.

(USED) CARS phase matching has been employed, with longitudinal spatial resolution of ~5 mm. For this geometry, the 532 nm pump/probe beam is enlarged and the center portion is blocked, creating an annulus, as shown in Fig. 2. This beam is then combined coaxially with the Stokes beam by a dichroic mirror and focused into the test section. After re-collimation, dichroic mirrors isolate the CARS signal beam, which is then directed into a 0.75-m spectrometer (see Fig. 2). At the spectrometer exit plane, a 2.3*x* relay lens magnification system is used to image the dispersed CARS signal onto an electron-multiplying charge coupled device (CCD) camera (Andor Newton). The combination of the 2.3*x* magnification and 3600 line/mm grating results in a spectral resolution of ~0.4 cm^{-1}, which is sufficient to partially resolve the rotational structure in the *Q*-branch of N_2. Details of data reduction, as well as rotational and vibrational temperature inference from the CARS spectra are discussed in Ref. [21].

3. Plasma chemistry model and nanosecond pulse discharge model

To obtain insight into kinetics of plasma/chemical fuel oxidation and ignition, we use a kinetic model developed in our previous work [15–20,22]. Briefly, the model incorporates nonequilibrium air plasma chemistry [23], expanded to include hydrocarbons and hydrogen dissociation processes in the plasma [16,24]. In the present work, the plasma chemical reaction list was also expanded to incorporate C_3H_8 dissociation reactions by electronically excited N_2 [25]. The dominant radical species generation processes in H_2-air and hydrocarbon-air and plasmas are listed in Table 1. The plasma chemistry model is coupled with one of two "conventional" hydrogen–oxygen chemistry mechanisms developed by Popov [24] and Konnov [25], and one of the three hydrocarbon chemistry mechanism, GRI Mech 3.0 [23], USC/Wang mechanism [24], or Konnov mechanism [29]. Note that the mechanisms have been developed and validated for relatively high-temperatures, significantly higher than found in the present experiments, and may well be inaccurate at the present conditions. Assessing applicability of these mechanisms, used as a starting point for development of a nonequilibrium plasma assisted combustion mechanism, is one of the objectives of the present work.

The list of air plasma chemistry processes and hydrogen–oxygen chemical reactions incorporated in the present model is given in Ref. [16] and Refs. [24,26], respectively. The species concentration equations are coupled with the two-term expansion Boltzmann equation for plasma electrons. The model incorporates the energy equation for the temperature on the discharge centerline [22] as well as quasi-one-dimensional flow equations, with heat transfer to the walls (dominant energy loss mechanism at the present conditions) included. The model is validated using measurements of O-atom concentration (TALIF) [15,16], temperature (rotational CARS) [19,20], OH concentration (LIF) and ignition time [17,18,22] in ns discharges in air, and mixtures of air and CH_4, C_2H_4, and H_2.

Key parameters controlling plasma chemistry in the ns pulse discharge include the reduced electric field, *E*/*N*, and coupled pulse energy. Energy coupled to the plasma using two different ns pulse generators, including the FID pulser used in the present work, was measured in air in a low-temperature cell outside of the furnace, over a wide range of pressures [30]. It has been shown that at P = 10–100 torr, coupled pulse energy is nearly independent of pulse repetition rate (at ν = 1–40 kHz), remains nearly constant during the pulse burst (up to ~100 pulses), and is proportional to discharge pressure, i.e., energy coupled per molecule remains constant. These experimental results are in good agreement with the analytic model of energy coupling in a ns pulse discharge [31], which incorporates key effects of pulsed breakdown and sheath development on the ns time scale. The model predicts pulse energy coupled to the plasma vs. pulse voltage waveform, discharge geometry, pressure, and temperature. Time-dependent reduced electric field in the plasma during the discharge pulse, predicted by the model of Ref. [31], is fairly complex, with *E*/*N* rapidly dropping during breakdown [30], which introduces an uncertainty in the "effective" *E*/*N* value at which energy is coupled to the plasma. In the present plasma chemistry model, *E*/*N* in the plasma is approximated as a Gaussian pulse with the same time constant as the experimental voltage waveform, and the peak corresponding to the breakdown value predicted by the ns discharge model [31], approximately $(E/N)_{peak}$ = 600 Td, with the coupled pulse energy of 1.25 mJ/pulse (0.46 meV/molecule). At the present conditions, the model predictions are not very sensitive to the effective *E*/*N* value. Reducing peak *E*/*N* by a factor of 3, to 200 Td, while keeping the pulse energy the same, results in a fairly modest increase of predicted OH number density after the burst, by approximately 20%. The uncertainty of the predicted coupled energy value is approximately ±50%, due to a significant uncertainty in the dielectric constant of high-temperature dielectric layers (Kalrez). In the experiment, the uncertainty is primarily due to the effect of corona discharges forming near the electrodes outside the test cell, which reduces the energy coupled to the plasma inside the cell. The value of 1.25 mJ/pulse, used in the present work, provides the best agreement with the data. Varying the pulse energy within the estimated uncertainty limit results in predicted [OH] variation by approximately ±20%.

It is necessary to point out that the plasma chemistry model used in this work also incorporates a set of NO_x formation and decay reactions (list of these reactions for air plasma is given in Ref. [16]). NO may affect radical species chemistry at low temperatures, primarily via recombination reaction $NO + O\ (+M) \rightarrow NO_2\ (+M)$, which reduces O atom number density. NO may also affect OH number density, e.g., via a rapid reaction $HO_2 + NO \rightarrow NO_2 + OH$. At the present conditions, the predicted NO mole fraction after the burst is of the order of ~150 ppm, significantly higher compared to OH mole fraction, ~10 ppm. However, varying NO

fraction in the initial fuel–air mixture in the range of 0–300 ppm resulted in a weak change of the predicted OH number density, by 1–2%. Therefore at the present low-temperature conditions, NO chemistry is not expected to play an important role in fuel oxidation kinetics.

4. OH LIF and LIF thermometry

4.1. Basics

Operating in linear excitation regime, the time-integrated fluorescence signal, S_f, can be expressed as follows:

$$S_f(v) = n_{OH} f_B b_{12} E \phi_J g(v) l \frac{\Omega}{4\pi} \beta. \quad (1)$$

where n_{OH} is OH number density (cm^{-3}); f_B is the Boltzmann factor for OH molecules in the absorbing state, calculated using the rotational energy term values for $X^2\Pi$ $v = 0$ state from Ref. [32]; $b_{12} = B_{12}/c$ is the Einstein absorption coefficient ($cm^2\ J^{-1}\ cm^{-1}$), taken from LIFBASE [33]; E is the laser energy (J); ϕ_J is the fluorescence quantum efficiency (or quantum yield); $g(v)$ is the normalized overlap integral ($1/cm^{-1}$), i.e., a convolution of laser lineshape and absorption lineshape; l is the path length of the laser sampled by the collection optics (cm); Ω is the solid angle of detection (sr); and β represents the overall conversion coefficient, which consists of the efficiency of the collection optics and response of the detection system. For (1,0) excitation, the quantum yield can be derived by integrating the rate equation over the entire LIF pulse, while also taking into account spontaneous emission (A_1 and A_0), electronic quenching (Q_1 and Q_0), and vibrational energy transfer (VET) from $v' = 1$ to $v' = 0$ (V_{10}):

$$\phi_J = \frac{\varepsilon_1 A_1 + \varepsilon_0 A_0 V_{10}/(A_0 + Q_0)}{V_{10} + A_1 + Q_1}. \quad (2)$$

In Eq. (2), ε_0 and ε_1 are signal collection efficiencies for emission from $v' = 0$ and $v' = 1$ of the $A^2\Sigma^+$ state, respectively, which account for differences in fluorescence trapping and spectral sensitivity of the detection system for different transitions. It should be noted that VET acts to redistribute the A-state population (from $v' = 1$ to $v' = 0$), and the equation can be simplified with the following two approximations that eliminate the dependence on the VET rate: (1) $A_0 + Q_0 \approx A_1 + Q_1$ (which is not unreasonable based on literature quenching rates, see Refs. [34,35]) and (2) $\varepsilon_0 A_0 \approx \varepsilon_1 A_1$ (also not unreasonable, see Ref. [33]). Thus,

$$\phi_J = \frac{\varepsilon_0 A_0}{A_0 + Q_0}. \quad (3)$$

In this work, the quantum yield is calculated from the measured fluorescence decay time, $\tau = 1/(A_0 + Q_0)$. We note that the quantum yield estimate for (1,0) excitation can be compared with measurements using A–X(0,0) excitation.

Without knowing the laser linewidth accurately, calculation of the normalized overlap integral in Eq. (1), $g(v)$, may result in significant uncertainty. In the present work, performing the excitation scan over an isolated transition, and integrating the fluorescence signal over a wide spectral range, $g(v)$ becomes unity, and therefore no knowledge of laser linewidth is required to reduce the data. In this case, Eq. (1) becomes

$$S_f = n_{OH} f_B b_{12} E \phi_J l \frac{\Omega}{4\pi} \beta. \quad (4)$$

For OH LIF thermometry, (1,0) excitation is preferred for better rejection of laser scattering. Rotational temperature is inferred from the slope of the Boltzmann fit of fluorescence intensities from the five excitation transitions listed in Section 2.

4.2. Calibration

In order to obtain a calibration factor for the LIF data taken using (1,0) excitation, experiments employing two of the four equivalence ratios for each fuel–air mixture listed in Section 2 were repeated using (0,0) excitation. These experiments have been conducted in the modified test cell with Brewster windows (see Section 2). Since VET is not involved in (0,0) excitation (assuming no upward VET from $v' = 0$ to $v' = 1$), the fluorescence quantum yield, calculated from the measured fluorescence decay time using Eq. (3), is more accurate. The rest of parameters in Eq. (4), necessary to calculate the absolute OH concentration, i.e., the product of l, Ω, and β, are determined from Rayleigh scattering, as follows:

$$S_{Rayleigh} = \frac{\varepsilon_R}{hc\nu} \left(\frac{\partial\sigma}{\partial\Omega}\right) l\Omega\beta \cdot (NE). \quad (5)$$

In Eq. (5), h is the Planck constant (J s); ν is the laser wavelength (cm^{-1}); c is the speed of light (cm/s); $\left(\frac{\partial\sigma}{\partial\Omega}\right)$ is the Rayleigh scattering differential cross section (cm^2/sr), calculated using dispersion relations for depolarization from Ref. [36] and for index of refraction from Ref. [37]; $N = P/kT$ is the gas number density (cm^{-3}); and ε_R is the collection efficiency of the Rayleigh scattering. By varying the pressure of a buffer gas (N_2 or air) inside the same test cell as used for OH LIF experiments, and/or the laser pulse energy, a linear plot of $S_{Rayleigh}$ vs. (NE) was obtained, the slope of which was used to calculate the collection constant, $l\Omega\beta$, in Eq. (5). Then, absolute OH concentrations were calculated for the (0,0) excitation cases. Finally, by comparing signal levels to those with known OH concentration, the rest of relative OH concentrations measured using (1,0) excitation were put on an absolute scale. This calibration scheme is discussed in greater detail in Ref. [38]. Based on a standard error propagation analysis, and by taking into account uncertainties in measured laser energy, inferred temperature, shot-to-shot signal variation, and uncertainties in the cross sections of various processes involved (absorption, emission, quenching, vibrational energy transfer, and Rayleigh scattering), the combined uncertainty in the OH number density is estimated to be ±20%.

5. Results and discussion

5.1. Discharge uniformity

Plasma uniformity is difficult to quantify but critical for isolating nonequilibrium chemistry effects from thermal heating occurring in filaments and hot spots. The approach used for sustaining diffuse, nearly zero-dimensional ns pulse discharges in a plane-to-plane geometry was discussed in detail in our previous work [18,22]. Before quantitative OH LIF measurements were performed, plasma uniformity was verified qualitatively by taking images employing an intensified charge-coupled device (ICCD) camera during individual discharge pulses. Time-resolved, broadband, single-shot images taken during a high voltage ns pulse discharge in air at $T_0 = 500$ K and $P = 50$ torr, using a PI-MAX ICCD camera and a UV lens (Sodern 100-mm f/2.8), are shown in Fig. 3. The camera gate is set at 490 ps and synchronized with the high voltage pulse generator to open during the last pulse in a 10-pulse discharge burst, with $t = 0$ representing the beginning of the pulse. The timing of the gate is indicated on the top of each image. The images capture primarily nitrogen second positive band emission, N_2 $C^3\Pi \rightarrow B^3\Pi$. From the images in Fig. 3, it is evident that the plasma is generated in the entire volume between the electrodes and remains diffuse and nearly uniform until it decays completely. Total emission intensity (a sum of intensity counts over all pixels in each ICCD image) decays very rapidly after each discharge pulse, on the time scale of a few ns, demonstrating that excited radiating species

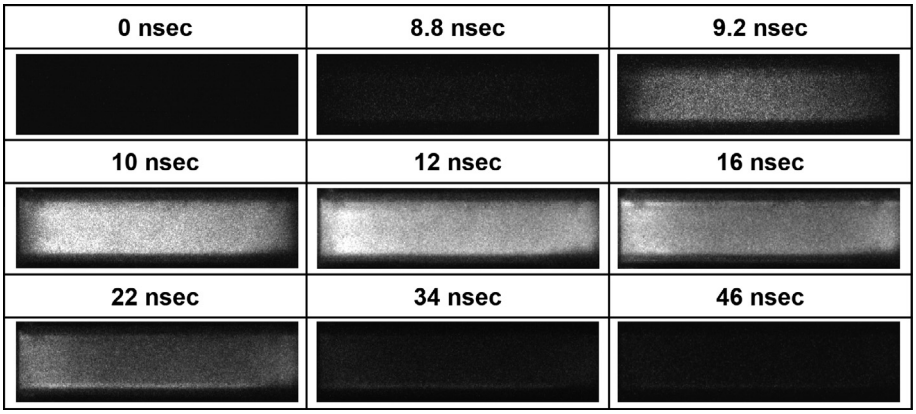

Fig. 3. Broadband single-shot ICCD images of the plasma during a single discharge pulse (pulse #10 in the burst) in air. $T_0 = 500$ K, $p = 50$ torr, $\nu = 10$ kHz. Camera gate = 490 ps, timing of the gate is shown on top of each image. Intensity of images taken at $t < 10$ ns is enhanced for illustrative purposes.

(mainly N_2 $C^3\Pi$ state) are quenched rapidly. Figure 4 shows ICCD images taken at the same conditions as in Fig. 3, through the window at the end of the flow channel. To isolate plasma emission from the reflections from the channel walls, images were taken with and without the discharge, and a rectangular region corresponding to the channel cross section (22 mm × 10 mm) was extracted from the original images, as shown in Fig. 4. Again, it can be seen that the plasma is diffuse and occupies the entire volume between the electrodes.

As discussed in our previous work [22], increasing pressure and/or adding H_2 or hydrocarbons to the air plasma makes the discharge less uniform and results in formation of well-defined filaments, due to development of ionization – heating instability. This effect is especially well pronounced in hydrocarbon-air mixtures at pressures of ~100 torr and above, although mild preheating to $T_0 = 400$–500 K reduces the nonuniformity considerably. Figure 5 shows ICCD images (50-ns exposure) of discharges in air, H_2-air ($\phi = 0.3$), and C_2H_4-air ($\phi = 0.3$) preheated to $T_0 = 500$ K, taken through the window in the end of the channel. These images illustrate that the plasma remains diffuse and filament-free at these conditions. As in Fig. 4, the images show the entire channel cross section (22 mm × 10 mm). Note, however, that ns pulse plasma-assisted ignition in CH_4-air and C_2H_4-air mixtures still exhibits a well-defined propagating flame front [22], such that near-homogeneous ignition could not be achieved. In the present work, this problem is circumvented by employing short discharge bursts (50 pulses at the pulse repetition rate of $\nu = 10$ kHz, far less than needed for ignition) and operating in fuel-lean mixtures, with the main emphasis of measuring OH number density in the plasma prior to ignition. Plasma uniformity at these conditions has been verified for three representative fuel–air mixtures (CH_4-, C_2H_4-, and H_2-air mixtures at $\phi = 0.3$), at three different pressures (100, 300 and 500 torr), as shown in Fig. 6. As discussed in Section 2, LIF signal is collected from the region in the center of the plasma approximately 1.5 cm long, about ¼ of the length of the discharge. This eliminates the effect of discharge nonuniformity that may be found near electrode edges at high pressures [22].

5.2. OH LIF thermometry and comparison to CARS temperature measurements

A typical excitation spectrum of the five OH A–X (1,0) transitions used in the present work is shown in Fig. 7. The spectrum is taken 2 μs after the end of the last pulse in an H_2-air mixture

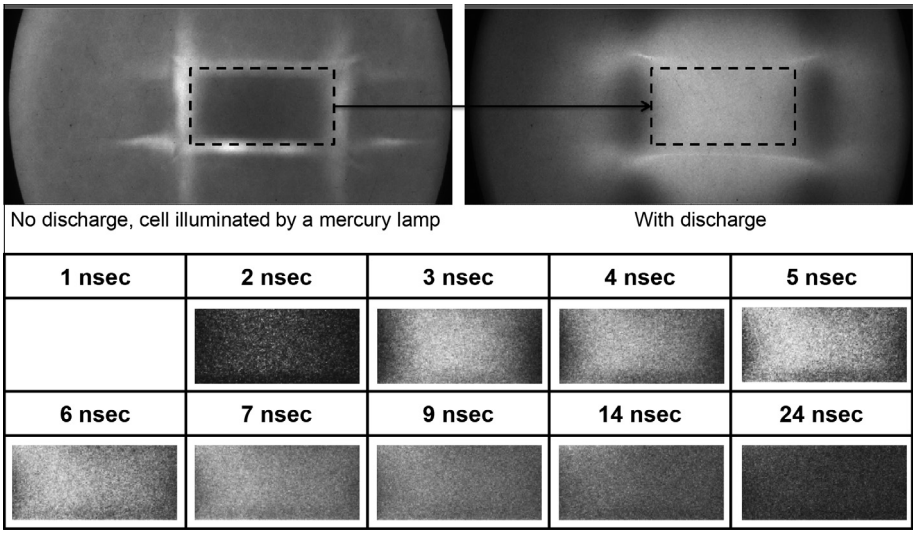

Fig. 4. Top: single shot ICCD images of the flow channel without the discharge and with the discharge, taken through the window at the end of the channel. Extracted region corresponds to the channel cross section (22 mm × 10 mm). Bottom: images of the plasma during a single discharge pulse (pulse #10 in the burst) in air at the conditions of Fig. 3, taken through the same window and showing the entire channel cross section. Camera gate 490 ps, timing of the gate is shown on top of each image.

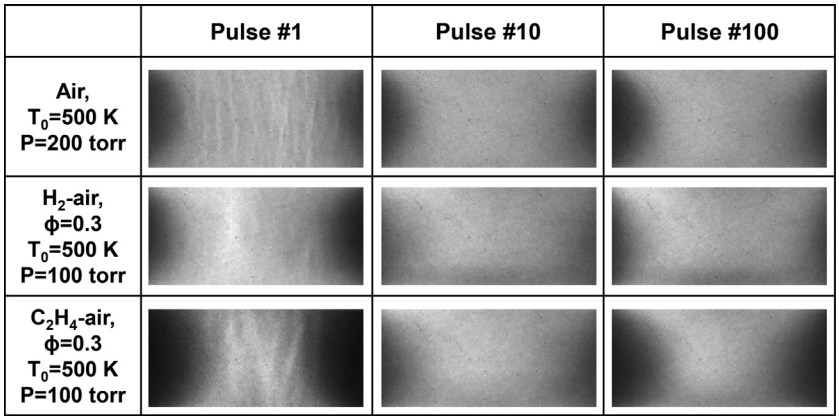

Fig. 5. Single shot ICCD images of the plasma in and fuel–air mixtures preheated to $T_0 = 500$ K, taken through the window in the end of the channel. $\nu = 10$ kHz, camera gate = 50 ns, images show the entire channel cross section (22 mm × 10 mm).

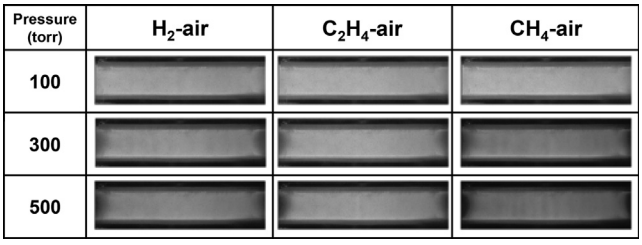

Fig. 6. Single shot ICCD images of the plasma in fuel–air mixtures illustrating discharge uniformity. $T_0 = 500$ K, $\phi = 0.3$, $\nu = 10$ kHz, pulse #10. Camera gate = 50 ns.

at $\phi = 0.12$, $T_0 = 500$ K, and $P = 100$ torr, excited by a $\nu = 10$ kHz, 50 pulse discharge burst. This is close to minimum time delay for which LIF signal is not affected by EMI from the discharge. In Fig. 7, each experimental data point represents a median of 60 laser shots taken at each scanning step. As discussed in our previous work [18], Voigt line shape profiles are used to fit the experimental spectra to isolate overlapping spectral lines, which appear in all Q-branch transitions. After isolating the main-branch transitions and integrating them over the same wavelength range, symmetric to the centerline wavelength, rotational temperature is inferred from the Boltzmann plot, such as shown in Fig. 8. Each of the excitation scans shown in Fig. 7 is repeated three times to improve accuracy. Only the major transitions are included in the Boltzmann fit. At some conditions, including the one shown in Fig. 8, data from the $P_1(1)$ and $Q_1(2)$ transitions deviate somewhat from the straight line formed by $Q_1(3)$, $Q_1(4)$ and $Q_1(5)$ transitions. If $P_1(1)$ and $Q_1(2)$ are removed from Fig. 8, the best fit rotational temperature would be $T_{rot} = 557 \pm 25$ K, which differs by 30 K from the best fit temperature obtained using a 5 rotational line fit ($T_{rot} = 587 \pm 27$ K). This relatively small discrepancy could be due to $P_1(1)$ line being relatively weak, as well as a strong overlap between $Q_1(2)$ with $Q_{21}(2)$ lines, which may introduce uncertainty in data processing and Voigt line fitting. Of course, some fitting error may be incurred with run to run variations (since there may in fact be some temperature variation from run to run). Nonetheless, this difference in best fit rotational temperature values is close to the statistical uncertainty (95% confidence interval) of the Boltzmann fit used for temperature inference. In most cases, transitions involving low rotational levels (e.g., $P_1(1)$ and $Q_1(2)$) are needed for better rotational temperature sensitivity.

Figure 9a shows a 100-shot accumulation N_2 ps CARS spectrum taken in air at $P = 100$ torr and $T_0 = 500$ K (without the plasma), along with the best-fit synthetic spectrum generated using the Sandia National Laboratories CARSFIT program [39]. The confidence interval of temperature inference was determined by taking 100 CARS spectra at these well-characterized conditions, 100-shot accumulation each. For each of these spectra, rotational temperature was inferred using a least squares fit synthetic spectrum calculated by CARSFIT. The best fit rotational temperature, $T = 486$ K, standard deviation, and 95% confidence interval, ~15 K at these reference conditions, were obtained from statistical analysis of these 100 temperature values. The relative uncertainty in rotational temperature is expected to improve with increasing

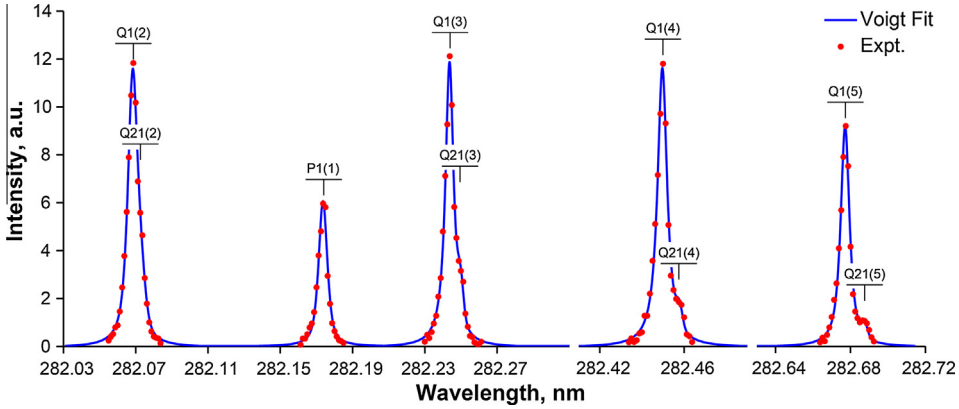

Fig. 7. Typical OH LIF excitation spectrum used for temperature measurements. Spectrum taken 2 μs after the last pulse in the burst ($\nu = 10$ kHz, 50 pulses). H_2-air, $T_0 = 500$ K, $P = 100$ torr, $\phi = 0.12$.

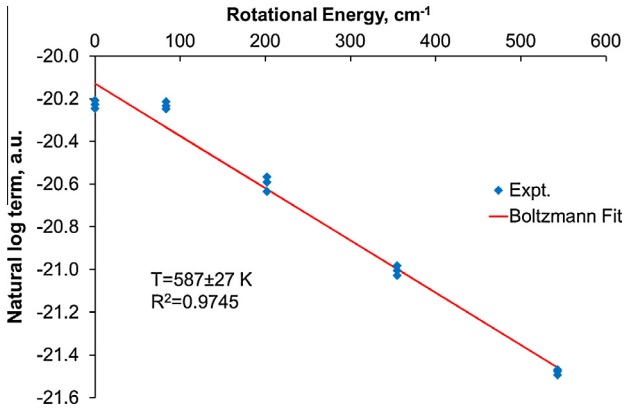

Fig. 8. Boltzmann plot obtained from the OH LIF excitation spectrum shown in Fig. 7 (H_2-air, T_0 = 500 K, P = 100 torr, ϕ = 0.12, ν = 10 kHz, 50 pulses). Best fit rotational temperature is T = 587 ± 27 K.

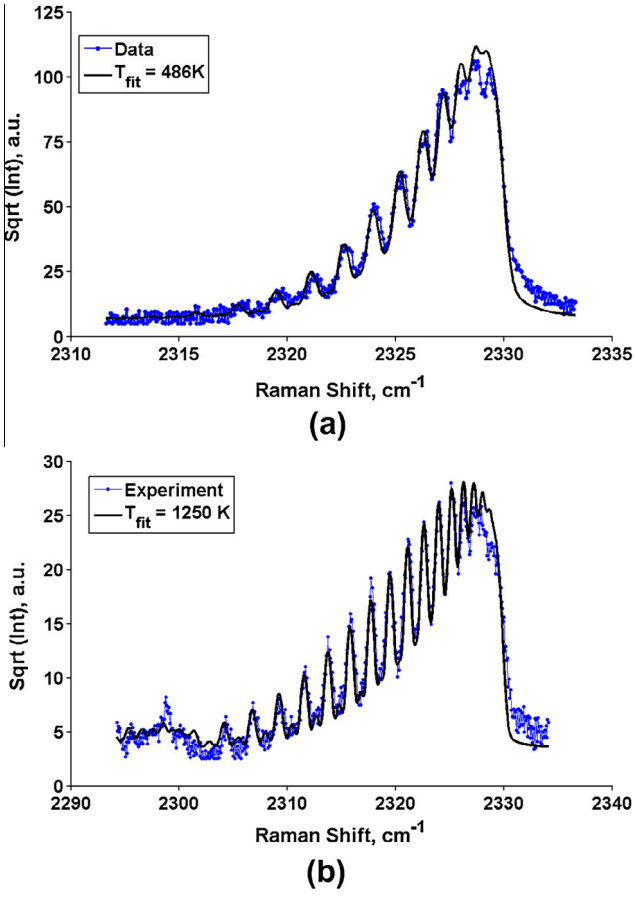

Fig. 9. (a) 100-Shot accumulation ps CARS spectrum in air at P = 100 torr and T_0 = 500 K, T_{fit} = 486 K, 95% confidence interval ~15 K and (b) 100-shot accumulation ps CARS spectrum in ϕ = 0.4 H_2 – air plasma at P = 92 torr during ignition, T_{fit} = 1250 K.

temperature due to increasing populations of higher rotational levels, which are more readily resolved in the Q-branch spectra. Figure 9b plots a 100-shot accumulation N_2 ps CARS spectrum taken in ϕ = 0.4 H_2-air plasma at P = 92 torr during ignition, and the best fit synthetic spectrum with T_{fit} = 1250 K. In Fig. 9b, $N_2(v = 1)$ vibrational band is also detected at Raman shifts below 2300 cm^{-1}. The two experimental spectra shown in Fig. 9 represent two extremes of the temperature observed in the present experiments, 500 K and 1250 K (during ignition). As can be seen, in both cases, the synthetic spectra are in good agreement with the experimental spectra. 100-shot accumulation CARS spectra were used to obtain each temperature value discussed below.

Figure 10 compares time-resolved rotational temperature measured by OH LIF in a C_2H_4-air mixture at ϕ = 0.09, T_0 = 500 K, P = 100 torr, after a ν = 10 kHz, 50-pulse discharge burst with rotational temperature measured by ps CARS at the same conditions. Temperatures measured by these two techniques are close to each other, showing that the temperature in the discharge increases by ΔT = 50–80 K (from the initial value of T_0 = 500 K) and remains nearly constant for up to 1 ms after the discharge burst. In fact, additional temperature measurements for very long delays after a 50-pulse burst, plotted in Fig. 12a and discussed below, demonstrated that the temperature remains approximately the same for up to ~10 ms after the burst. These results are also consistent with the temperature rise in the discharge predicted by the kinetic model at these conditions (equaling $\Delta T \sim$ 100 K), also shown in Fig. 10. A relatively modest temperature rise in the discharge, as well as its weak dependence on the equivalence ratio are also observed in other fuel–air mixtures at the same initial temperature, pressure, and discharge burst duration, as shown in Fig. 11. The temperature rise during the burst, averaged over different fuels and equivalence ratios, is $\Delta T_{avg} \approx$ 70 K. Again, the temperatures derived from OH LIF data (triangles, Fig. 11) are consistent with the CARS results (squares) and fuel–air plasma chemistry model predictions (lines). Based on these results, the same temperature value, averaged over different fuels and equivalence ratios, T_{avg} = 570 K, was used to calculate the Boltzmann factor to infer absolute, time-resolved OH number densities from the LIF data.

Figure 12a plots temperatures measured by CARS after the discharge burst in H_2-air at ϕ = 0.4, T_0 = 500 K, P = 92 torr, and ν = 10 kHz, for three different burst durations (50–120 pulses). Also plotted in Fig. 12a are the model predictions at these conditions (solid lines), which are in very good agreement with CARS data up to fairly long delay times after the burst, 20 ms, although the model again systematically overpredicts the temperature at the end of the discharge burst, by about 50 K. From the results shown in Fig. 12a, it is apparent that threshold temperature at the end of the discharge burst, above which ignition occurs, is $T_f \approx$ 700 K, approximately 200 K below the normal autoignition temperature [22]. This result confirms our previous temperature measurements by N_2 emission spectroscopy [22], although the results of Ref. [22] were not spatially resolved and had more uncertainty. Below this threshold, ignition does not occur and the temperature gradually decays to pre-excitation baseline value of T_0 = 500 K. In addition,

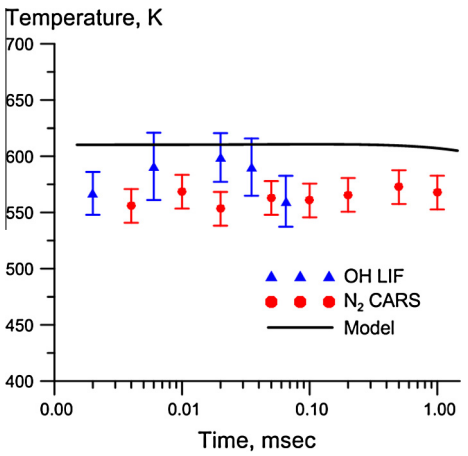

Fig. 10. Comparison of temperatures measured by OH LIF and by CARS after a ν = 10 kHz, 50-pulse discharge burst in a C_2H_4-air mixture at T_0 = 500 K, P = 100 torr, ϕ = 0.09.

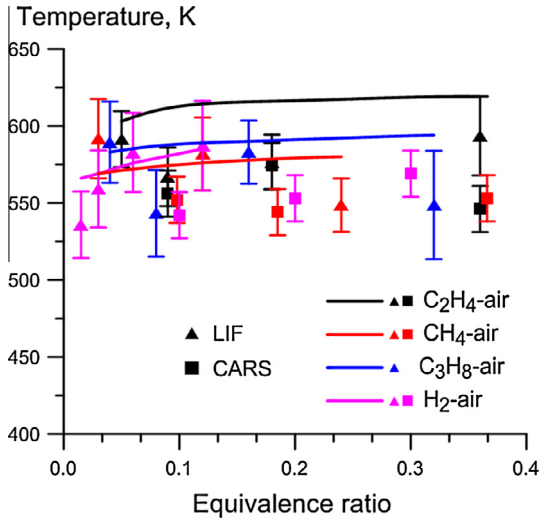

Fig. 11. Comparison of temperatures measured by OH LIF and by CARS in a ν = 10 kHz, 50-pulse discharge burst (2 μs after the last pulse) in different fuel–air mixtures at T_0 = 500 K, P = 100 torr. Model predictions are shown as solid lines.

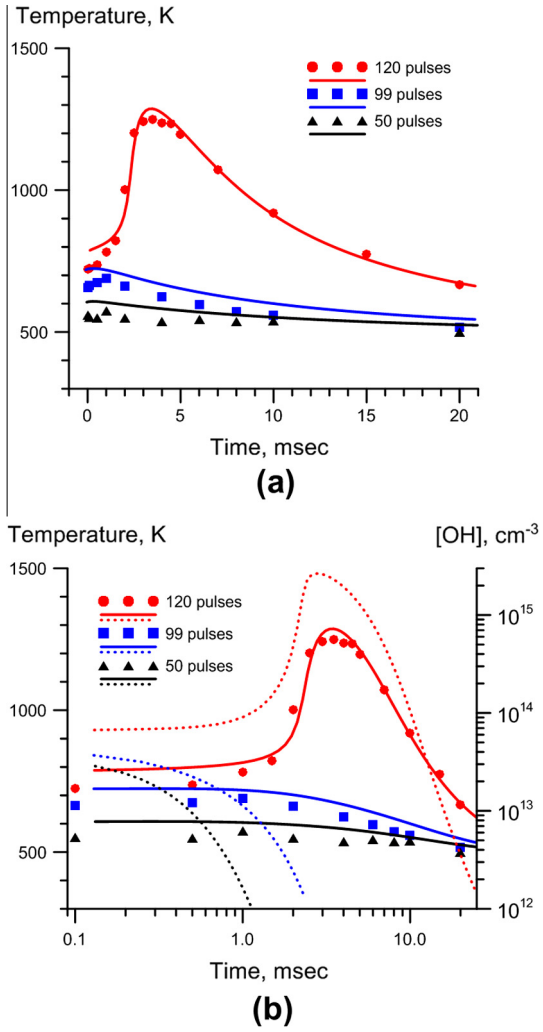

Fig. 12. Comparison of ps CARS temperature measurements after the discharge burst in a ϕ = 0.4 H_2-air mixture at T_0 = 500 K, P = 92 torr and ν = 10 kHz with kinetic modeling calculations, for different burst durations (50–120 pulses). Plot (b) is a semi-log graph (for the time axis) of plot (a) with the addition of OH number density predicted by the model. Model predictions are shown as lines. Solid lines, temperature; dashed lines, OH number density.

Fig. 12b plots the same temperatures vs. time as a semi-log graph, along with OH concentrations predicted by the model (shown by dashed lines). It can be seen that below ignition threshold, OH generated during the discharge burst also gradually decays and does not exhibit an overshoot typical for ignition.

Although CARS measurements demonstrated that fairly significant vibrational excitation of nitrogen occurs in a ν = 10 kHz ns pulse burst discharge sustained in the present cell in room temperature air [22], N_2 vibrational temperature measured in preheated air (T_0 = 500 K) was quite low, $T_v(N_2) \approx 850$ K for 50 pulses and $T_v(N_2) \approx 1050$ K for 100 pulses, as shown in Fig. 13. In fuel–air mixtures, N_2 vibrational temperature after a 50-pulse burst was even lower, near the detection limit, $T_v(N_2) \approx 600$–700 K. This demonstrates that at the present experimental conditions, vibrational nonequilibrium of excited fuel–air mixtures is not a significant factor. Since estimated characteristic decay time of excited electronic states of nitrogen at the present conditions is quite short, $\tau \sim 1$ μs for $N_2(A^3\Sigma)$, and even shorter for $N_2(B^3\Pi)$, $N_2(C^3\Pi)$ and $N_2(a'^1\Sigma)$ states, chemical kinetics of fuel–air mixtures on longer time scales is dominated by "conventional" chemical reactions among radical species generated in the discharge. This lends the present experiment to studies of radical reaction kinetics at relatively low temperatures, ranging from room temperature to ignition temperature.

5.3. OH number density after the discharge

Figure 14 plots absolute, time-resolved [OH] measured in lean H_2-air mixtures at T_0 = 500 K and P = 100 torr vs. time delay after a ν = 10 kHz, 50-pulse discharge burst, at different equivalence ratios (ϕ = 0.015–0.12). Rotational temperatures measured by LIF thermometry at the end of the burst (time delay 2 μs after the end of the last pulse in the discharge burst) at these conditions are also shown in Fig. 14 (circled). It can be seen that peak [OH] after the burst, $(3.0–3.6)\cdot10^{13}$ cm^{-3}, is not sensitive to the equivalence ratio in this range. Also, there is essentially no transient [OH] rise after the burst. The fairly long [OH] decay time, ~0.5–1.0 ms, shows that OH accumulates during the 10 kHz burst (tine interval between the pulses of 0.1 ms), consistent with our previous results in H_2-air at discharge pulse repetition rate of ν = 40 kHz [13]. As discussed above, temperature at the end of the discharge burst is not sensitive to the equivalence ratio and delay time after the discharge (see Figs. 10 and 11) and remains within the range of T = 540–580 K (see Fig. 14).

Figure 14 also compares kinetic model predictions with the experimental results, using two different "conventional" H_2-air

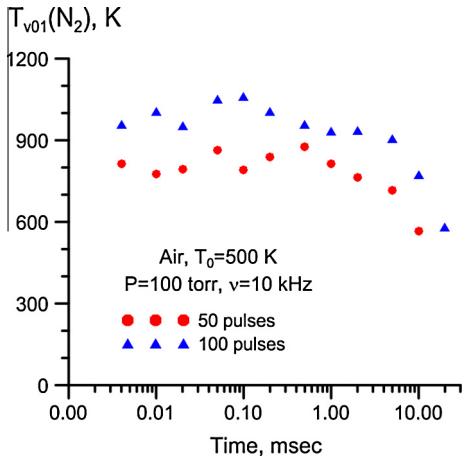

Fig. 13. Vibrational temperature of nitrogen measured by CARS after a ν = 10 kHz discharge burst in air T_0 = 500 K, P = 100 torr (50 and 100 pulses).

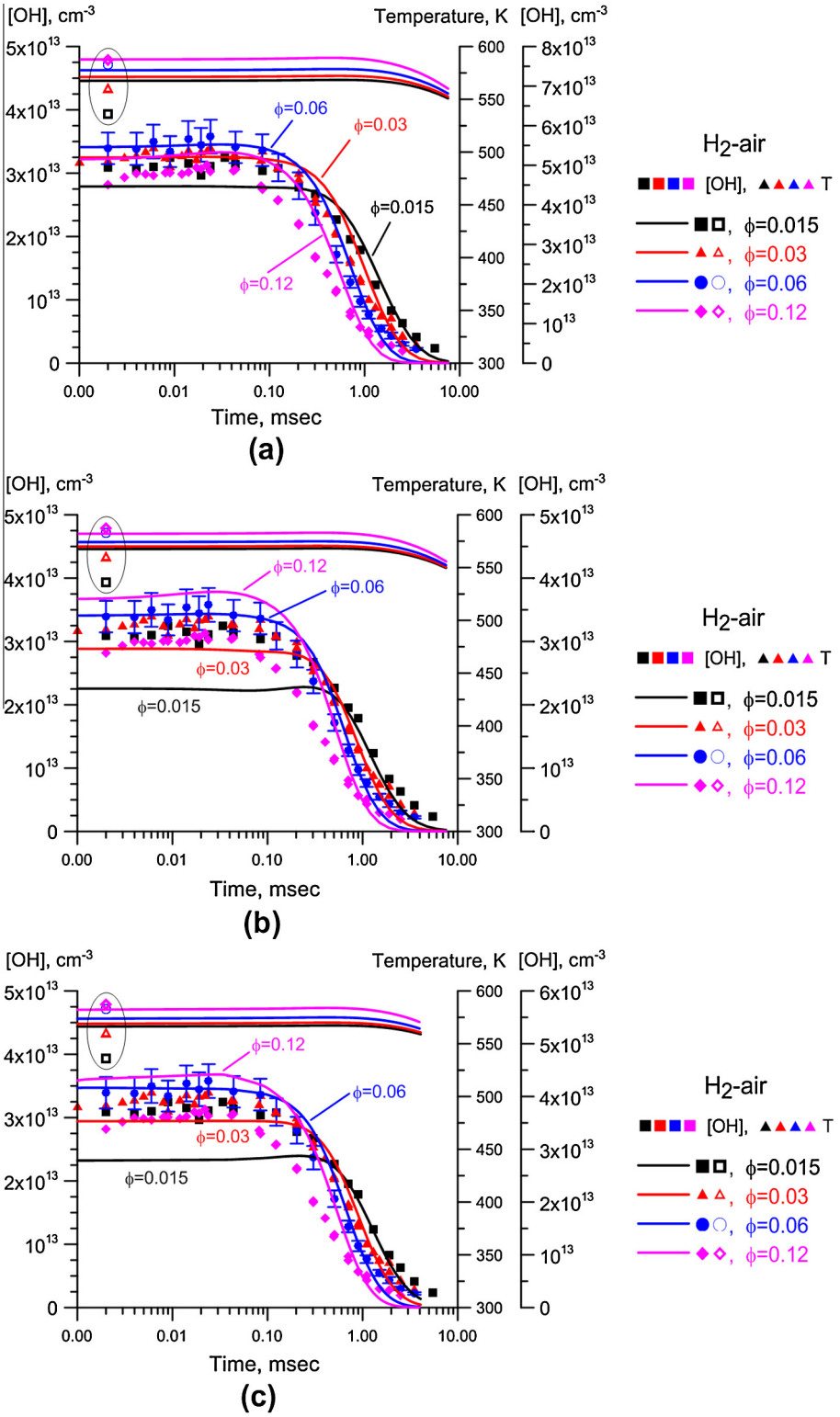

Fig. 14. Comparison of experimental (y-axis on the left) and predicted (y-axis on the right) time-resolved, absolute OH number densities after a $\nu = 10$ kHz, 50-pulse discharge burst in H_2-air mixtures at $T_0 = 500$ K, $P = 100$ torr, and different equivalence ratios. Data points for temperatures measured at the end of the burst (time delay 2 μs) are circled. (a) Popov mechanism, (b) Konnov mechanism and (c) Konnov mechanism with modified rate of reaction OH + O → H + O_2.

chemistry mechanisms developed by Popov [24] (Fig. 14a) and Konnov [26] (Fig. 14b). Note that the model predictions for [OH] are plotted using the vertical axis on the right-hand side of the figures, while the experimental data are shown using the vertical axis on the left-hand side. As can be seen, the Popov mechanism matches weak dependence of [OH] on the equivalence ratio (by 50–60%) but consistently overpredicts absolute [OH] and somewhat overpredicts the [OH] decay time at the higher equivalence ratio of $\phi = 0.12$ (see Fig. 14a). On the other hand, the Konnov mechanism matches absolute [OH] concentration as well as decay

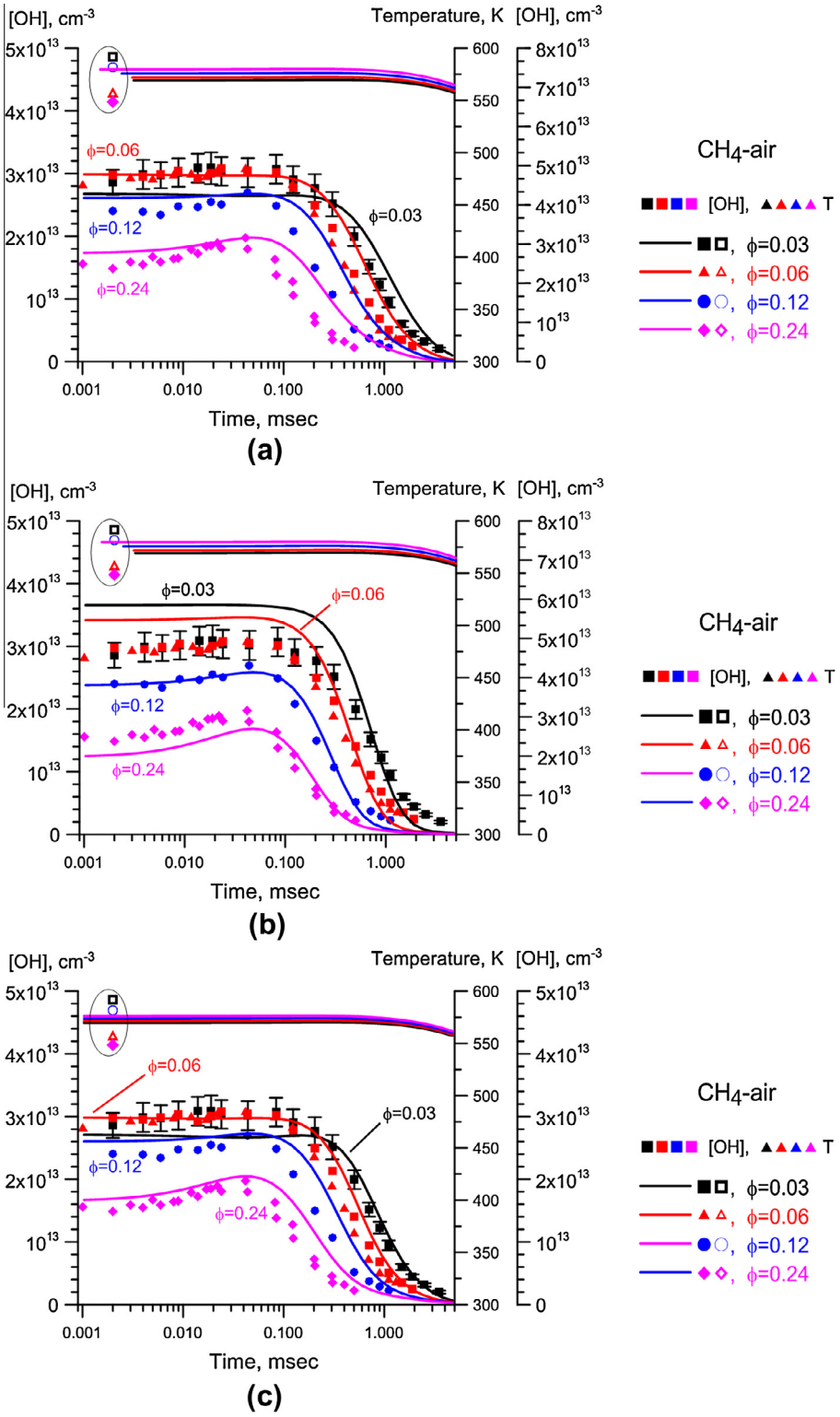

Fig. 15. Comparison of experimental (y-axis on the left) and predicted (y-axis on the right) time-resolved, absolute OH number densities after a $\nu = 10$ kHz, 50-pulse discharge burst in CH_4-air mixtures at $T_0 = 500$ K, $P = 100$ torr, and different equivalence ratios. Data points for temperatures measured at the end of the burst (time delay 2 μs) are circled. (a) GRI 3.0 mechanism, (b) USC/Wang mechanism and (c) Konnov mechanism.

time (except at $\phi = 0.12$) but shows a somewhat greater dependence of peak [OH] on the equivalence ratio than seen in the experimental results. Kinetic sensitivity analysis has shown that the difference between the two mechanisms is almost entirely due to the difference in the rate coefficients of reaction $O + OH \rightarrow H + O_2$, $k_r = 1.2 \times 10^{-11}$ cm^3/s [19] and $k_r = 5.3 \times 10^{-11}$ cm^3/s [26] at $T = 500$ K (note that the former value violates the detailed balance, since the rate coefficients used for the reaction $H + O_2 \rightarrow O + OH$ in Refs. [20,26] are close, $k_f = 5.3 \times 10^{-17}$ cm^3/s and $k_f = 4.9 \times 10^{-17}$ cm^3/s, respectively). The use of the rate coefficient recommended

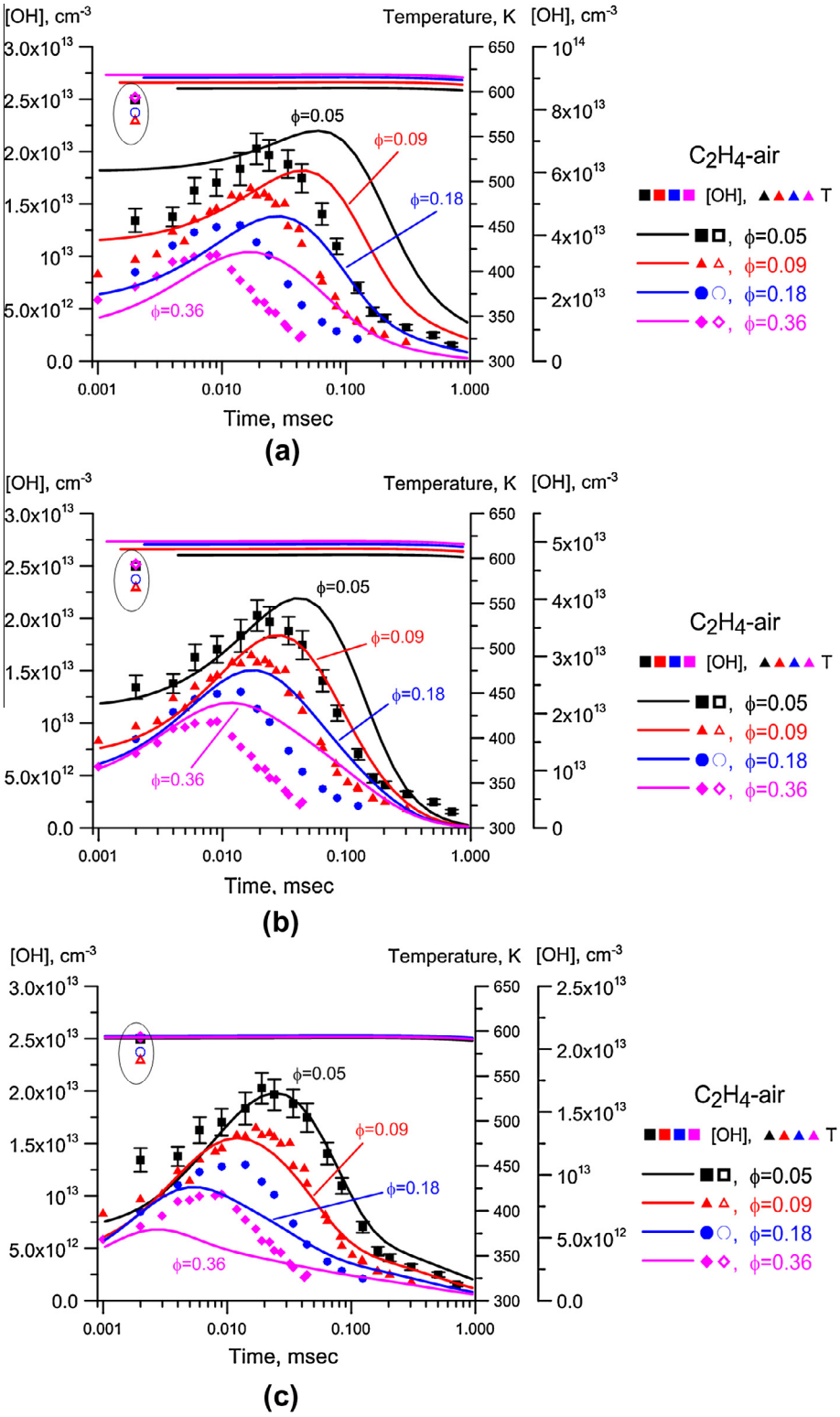

Fig. 16. Comparison of experimental and predicted time-resolved, absolute OH number densities after a $\nu = 10$ kHz, 50-pulse discharge burst in C_2H_4-air mixtures at $T_0 = 500$ K, $P = 100$ torr, and different equivalence ratios. Data points for temperatures measured at the end of the burst (time delay 2 μs) are circled. (a) GRI 3.0 mechanism, (b) USC/Wang mechanism and (c) Konnov mechanism.

in the recent review [40], $k_r = 3.5 \times 10^{-11}$ cm^3/s ($k_f = 3.3 \times 10^{-17}$ cm^3/s) in the Konnov mechanism results in [OH] overprediction by approximately 25%, with other changes being insignificant (see Fig. 14c).

The results in lean CH_4-air mixtures are shown in Fig. 15. Unlike in H_2-air mixtures, peak [OH] after the burst is reduced as the equivalence ratio increased, by about 50% between $\phi = 0.03$ and $\phi = 0.24$. Similar to H_2-air mixtures, almost no transient [OH]

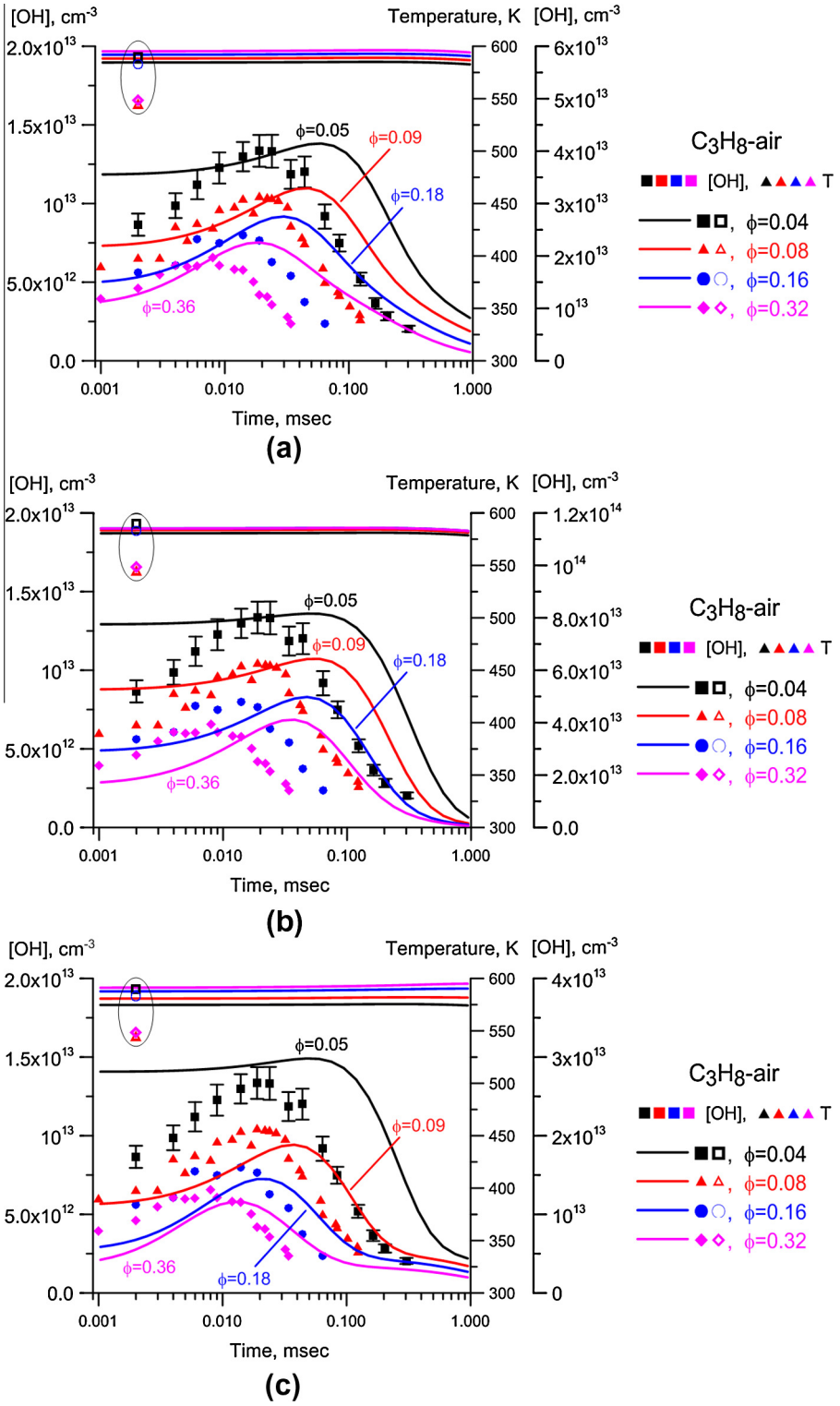

Fig. 17. Comparison of experimental and predicted time-resolved, absolute OH number densities after a $v = 10$ kHz, 50-pulse discharge burst in C_3H_8-air mixtures at $T_0 = 500$ K, $P = 100$ torr, and different equivalence ratios. Data points for temperatures measured at the end of the burst (time delay 2 μs) are circled. (a) GRI 3.0 mechanism, (b) USC/Wang mechanism and (c) Konnov mechanism.

increase is observed, except for a modest rise at $\phi = 0.24$. The [OH] decay time in CH_4-air is somewhat shorter than in H_2-air, ranging from ~1 ms at $\phi = 0.03$ to ~0.2 ms at $\phi = 0.24$. Again, this suggests fairly significant OH accumulation during the discharge burst at the pulse repetition rate of $v = 10$ kHz. At the higher equivalence ratio, $\phi = 0.24$, a modest transient [OH] overshoot after the burst is apparent. [OH] after the discharge burst predicted by two "conventional" hydrocarbon-air chemistry mechanisms, GRI 3.0 [27] and USC/Wang [28], are relatively close to each other (see Fig. 15a and b), both exceeding peak measured [OH] by 60–100%. Both mechanisms reproduce weak transient [OH] rise in higher equivalence ratio mixtures, with Wang mechanism showing better

agreement with [OH] decay after the burst. The Konnov mechanism, on the other hand, matches absolute [OH], the weak transient rise, and the [OH] decay relatively well (see Fig. 15c). Comparison with the modeling calculations shows clearly that both peak [OH] and decay time reduction at higher equivalence ratios are primarily due to increase in net rate of radical removal via fuel oxidation reactions, since coupled discharge pulse energy and the net rate of radical generation are nearly independent of the equivalence ratio.

An additional series of calculations was done to evaluate the potential effect of hydrocarbon impurities in 99.0% pure methane. The presence of trace hydrocarbon species, such as such as ethylene, acetylene, and ethane, rapidly reacting with the radicals generated in the plasma (primarily with O and H atoms) may affect kinetics of plasma-assisted methane oxidation, since low-temperature rates for CH_4 reactions with O and H atoms are fairly slow. The upper bound effect of these species on low-temperature methane oxidation kinetics was estimated using kinetic modeling calculations, by adding 1% of C_2H_2, C_2H_4, C_2H_6, or CO to CH_4. The results demonstrate that C_2H_2, C_2H_4, or C_2H_6 addition results in less than 0.5% difference in predicted peak temperature, less than 1% difference in predicted quasi-steady-state OH number density at the end of the burst, and approximately 5% difference (reduction) in predicted OH decay time after the burst. As expected, OH decay time reduction is primarily due to significantly more rapid reaction rates of radicals with these hydrocarbon additives. Adding 1% CO did not result in a detectable change of the predicted temperature or OH number density at the present conditions. Although higher methane purity is indeed desired in the future experiments, we conclude that the effect of hydrocarbon impurities (at or below 1% in concentration) in methane on low-temperature methane oxidation kinetics is fairly minor.

Figure 16 plots the results in lean C_2H_4-air mixtures. It can be seen that in the entire range of equivalence ratios, [OH] after the burst first increases, by up to 60%, before eventually decaying. Similar to the results in CH_4-air mixtures, increasing the equivalence ratio reduces peak transient [OH] after the burst by approximately a factor of 2, from $\approx 2 \times 10^{13}$ cm^{-3} at $\phi = 0.05$ to $\approx 1 \times 10^{13}$ cm^{-3} at $\phi = 0.36$ (see Fig. 16). Finally, [OH] decay time is much shorter than in H_2-air and CH_4-air and is reduced considerably as the equivalence ratio is increased, from ~0.1 ms at $\phi = 0.05$ to ~0.03 ms at $\phi = 0.36$. This shows that no significant OH accumulation occurs during the discharge burst, since [OH] decay time is comparable with time delay between the pulses in a 10 kHz burst. Again, these trends (both peak [OH] and decay time reduction) are due to more rapid net rate of radical removal via fuel oxidation reactions at the higher equivalence ratio. As can be seen, GRI 3.0 mechanism overpredicts both peak [OH] and decay time, by a factor of 3–4 (see Fig. 16a). The USC/Wang mechanism performs noticeably better, although peak [OH] and decay time are still underpredicted by about a factor of 2 (except at higher equivalence ratio, $\phi = 0.36$, where the model underpredicts the decay time by about a factor of 4, see Fig. 16b). Finally, the Konnov mechanism reproduces both peak [OH] and its decay in very lean mixtures well, although the agreement is not as good as the equivalence ratio is increased (see Fig. 16c). In this case, peak [OH] at higher equivalence ratios ($\phi = 0.18$ and $\phi = 0.36$) is underpredicted because the net rate of C_2H_4 oxidation process, initiated by C_2H_4 + O reactions, is overpredicted.

Based on the comparison of the present experimental results with kinetic modeling, the Konnov mechanisms for H_2-air, CH_4-air, and C_2H_4-air show better overall agreement with the data, compared to the Popov, GRI 3.0, and USC/Wang mechanisms. Note that kinetic modeling shows that significant transient [OH] rise after the burst, observed in C_2H_4-air, is not due to chain branching processes, which remain insignificant at these low temperatures. In fact, the transient rise in [OH] is produced primarily by O and H atoms generated by electron impact and by quenching of electronically excited nitrogen during and immediately after the last pulse in the burst (within ~1 μs [14]).

The experimental results in C_3H_8-air are very similar to those in C_2H_4-air (compare Figs. 16 and 17). In both fuel–air mixtures, peak [OH] is reduced as the equivalence ratio is increased, exhibiting a transient rise after the burst, and the [OH] decay rates in these two fuel–air mixtures are similar. However, kinetic modeling significantly overpredicts peak [OH] (by a factor of 3 for GRI 3.0, a factor of 6 for USC/Wang, and a factor of 2 for Konnov). Also, [OH] decay time is overpredicted considerably by all three mechanisms, and the significant transient rise in the lean mixture ($\phi = 0.04$) is not reproduced by any of them. In particular, predictions from the Konnov mechanism, which performs relatively well in H_2-air, CH_4-air, and C_2H_4-air, are at variance with the experimental results in C_3H_8-air.

We believe that these differences are primarily due to uncertainties in "conventional" C_3 chemical reaction pathways and rates. Indeed, the fuel fraction in the leanest C_3H_8-air mixture tested ($\phi = 0.04$) is only 0.18% (compared to 21% of air), suggesting that dominant plasma chemical radical generation processes occur during electron impact excitation and quenching of excited N_2 and O_2, within ~1 μs after the burst. Kinetics of these processes appear to be captured by the present plasma chemical model (using Konnov mechanism) relatively well, since the model predictions in very lean H_2-air, CH_4-air, and C_2H_4-air are close to the experiment values. Thus, the present data show the need for development of an accurate, predictive plasma chemistry/fuel chemistry kinetic model that would be applicable to fuels C_3 and higher. Also, tracing the cause of the differences between different fuel–air kinetic mechanisms to individual species and reactions requires detailed sensitivity analysis, which will be undertaken in our future work.

6. Summary

In the present work, calibrated OH Laser Induced Fluorescence (LIF) is used for time-resolved temperature and time-resolved, absolute OH number density measurements in fuel–air mixtures in a nanosecond (ns) pulse discharge cell/plasma flow reactor. Relative OH concentrations are put on an absolute scale by calibrating the optical collection constant using Rayleigh scattering. Rotational temperature is inferred from OH LIF excitation spectra using 5 different excitation transitions. Rotational temperature and N_2 vibrational temperature in the reactor have also been measured using broadband, picosecond Coherent Anti-Stokes Raman Spectroscopy (CARS) diagnostics. The premixed fuel–air flow in the reactor is excited by a repetitive ns pulse discharge in a plane-to-plane geometry, operated at a high pulse repetition rate, $\nu = 10$ kHz. The experiments are conducted in lean, slowly flowing H_2-air, CH_4-air, C_2H_4-air, and C_3H_8-air mixtures preheated to $T_0 = 500$ K in a tube furnace, at a pressure of $P = 100$ torr. In most of the present measurements, the discharge burst duration was limited to 50 pulses, insufficient to produce plasma-assisted ignition. The discharge uniformity in air and fuel–air flows has been verified using sub-ns-gated images from an intensified camera demonstrating that a diffuse, volume filling, uniform plasma is sustained in the entire range of operating conditions, at pressures of up to $P = 500$ torr.

The results demonstrate that rotational temperatures inferred from OH LIF spectra and partially rotationally resolved CARS spectra are in good agreement, providing additional validation to OH LIF thermometry diagnostics used in the present paper, as well as in our previous work [13]. Temperatures at the end of the discharge burst, measured by these two techniques, are in the range of $T = 550$–580 K, indicating a modest temperature rise of 50–80 K

occurs in the discharge burst, consistent also with kinetic modeling predictions. The temperature after the burst remains essentially unchanged, for up to 10 ms delay. N_2 vibrational temperatures inferred from CARS measurements are quite low, $T_v \approx 850$ K in air and $T_v \approx 600$–700 K in fuel–air after a 50-pulse burst, demonstrating that vibrational nonequilibrium is not a significant factor at the present conditions.

The measured, time-resolved, absolute OH number density demonstrates that OH generated in C_2H_4-air and C_3H_8-air mixtures is highest in very lean mixtures and is reduced by about a factor of 2 as the equivalence ratio is increased by a factor of ~8, from $\phi = 0.05$ to 0.36 for C_2H_4-air mixture and from $\phi = 0.04$ to 0.32 for C_3H_8-air mixture. In these two fuels, transient OH overshoot after the discharge burst, by up to a factor of 2, is detected. No significant overshoot is observed in CH_4-air and in H_2-air mixtures, however. In CH_4-air mixtures, OH concentration is also reduced as the equivalence ratio is reduced, but in H_2-air mixtures, OH concentration after the burst is nearly independent of the equivalence ratio. OH decay rate after the burst in C_2H_4-air and C_3H_8-air occurs on the time scale of ~0.02–0.1 ms, suggesting little accumulation during the burst of pulses. In CH_4-air and H_2-air, however, the OH decays within ~0.1–1.0 ms and ~0.5–1.0 ms, respectively, suggesting significant OH accumulation in lean mixtures during the burst.

The experimental results are compared with kinetic modeling calculations using a plasma/fuel chemistry model employing several different "conventional" H_2-air and hydrocarbon-air chemistry mechanisms. Based on this comparison, kinetic mechanisms for H_2-air, CH_4-air, and C_2H_4-air developed by A. Konnov show better overall agreement with the experimental results, compared to H_2-air mechanism developed by Popov, as well as the GRI 3.0 and USC/Wang mechanisms. In C_3H_8-air, however, none of the hydrocarbon chemistry mechanisms agrees well with the data. The present results show the need for development of an accurate, predictive low-temperature plasma chemistry/fuel chemistry kinetic model applicable to fuels C_3 and higher.

Acknowledgments

This work is supported by the U.S. Air Force Office of Scientific Research MURI "Fundamental Aspects of Plasma Assisted Combustion" Chiping Li – Technical Monitor.

References

[1] F. Wang, J.B. Liu, J. Sinibaldi, C. Brophy, A. Kuthi, C. Jiang, P. Ronney, M.A. Gundersen, IEEE Trans. Plasma Sci. 33 (2005) 844–849.
[2] S.V. Pancheshnyi, D.A. Lacoste, A. Bourdon, C.O. Laux, IEEE Trans. Plasma Sci. 34 (2006) 2478–2487.
[3] A. Bao, Yu.G. Utkin, S. Keshav, G. Lou, I.V. Adamovich, IEEE Trans. Plasma Sci. 35 (2007) 1628–1638.
[4] A. Dutta, Z. Yin, I.V. Adamovich, Combust. Flame 158 (2011) 1564–1576.
[5] H. Do, S.-K. Kim, M.G. Mungal, M.A. Cappelli, Combust. Flame 157 (2010) 2298–2305.
[6] S.A. Bozhenkov, S.M. Starikovskaia, A.Yu. Starikovskii, Combust. Flame 133 (2003) 133–146.
[7] S.M. Starikovskaia, E.N. Kukaev, A.Yu. Kuksin, M.M. Nudnova, A.Yu. Starikovskii, Combust. Flame 139 (2004) 177–187.
[8] G. Pilla, D. Galley, D.A. Lacoste, F. Lacas, D. Veynante, C.O. Laux, IEEE Trans. Plasma Sci. 34 (2006) 2471–2477.
[9] W. Kim, H. Do, M.G. Mungal, M.A. Cappelli, IEEE Trans. Plasma Sci. 34 (2006) 2545–2551.
[10] C. Cathey, J. Cain, H. Wang, M.A. Gundersen, C.D. Carter, M. Ryan, Combust. Flame 154 (2008) 715–727.
[11] W. Kim, M.G. Mungal, M.A. Cappelli, Combust. Flame 157 (2010) 374–383.
[12] L. Wu, J. Lane, N.P. Cernansky, D.L. Miller, A.A. Fridman, A.Yu. Starikovskiy, Proc. Combust. Inst. 33 (2011) 3219–3224.
[13] W. Sun, M. Uddi, T. Ombrello, S.H. Won, C. Carter, Y. Ju, Proc. Combust. Inst. 33 (2011) 3211–3218.
[14] W. Sun, M. Uddi, S.H. Won, T. Ombrello, C. Carter, Y. Ju, Combust. Flame 159 (2012) 221–229.
[15] M. Uddi, N. Jiang, E. Mintusov, I.V. Adamovich, W.R. Lempert, Proc. Combust. Inst. 32 (2009) 929–936.
[16] M. Uddi, N. Jiang, I.V. Adamovich, W.R. Lempert, J. Phys. D: Appl. Phys. 42 (2009) 075205.
[17] I. Choi, Z. Yin, I.V. Adamovich, W.R. Lempert, IEEE Trans. Plasma Sci. 39 (2011) 3288–3299.
[18] Z. Yin, I.V. Adamovich, W.R. Lempert, Proc. Combust. Inst. 34 (2013) 3249–3258.
[19] Y. Zuzeek, I. Choi, M. Uddi, I.V. Adamovich, W.R. Lempert, J. Phys. D: Appl. Phys. 43 (2010) 124001.
[20] Y. Zuzeek, S. Bowman, I. Choi, I.V. Adamovich, W.R. Lempert, Proc. Combust. Inst. 33 (2011) 3225–3232.
[21] A. Montello, Z. Yin, D. Burnette, I.V. Adamovich, W.R. Lempert, AIAA Paper 2012-3180, in: 43rd AIAA Plasmadynamics and Laser Conference, 25–28 June, 2012, New Orleans, LA.
[22] Z. Yin, K. Takashima, I.V. Adamovich, IEEE Trans. Plasma Sci. 39 (2011) 3269–3282.
[23] I.A. Kossyi, A.Yu. Kostinsky, A.A. Matveyev, V.P. Silakov, Plasma Sources Sci. Technol. 1 (1992) 207–220.
[24] N.A. Popov, Plasma Phys. Rep. 34 (2008) 376–391.
[25] N. Moreau, S. Pasquiers, N. Blin-Simiand, L. Magne, F. Jorand, C. Postel, J.-R. Vacher, J. Phys. D: Appl. Phys. 43 (2010) 285201.
[26] A. Konnov, Combust. Flame 152 (2008) 507–528.
[27] G.P. Smith, D.M. Golden, M. Frenklach, N.W. Moriarty, B. Eiteneer, M. Goldenberg, C.T. Bowman, R.K. Hanson, S. Song, W.C. Gardiner, Jr., V.V. Lissianski, Z. Qin, <http://www.me.berkeley.edu/gri_mech/>.
[28] H. Wang, X. You, A.V. Joshi, S.G. Davis, A. Laskin, F. Egolfopoulos, C.K. Law, USC Mech Version II. High-Temperature Combustion Reaction Model of H_2/CO/C_1-C_4 Compounds, May 2007, <http://ignis.usc.edu/USC_Mech_II.htm>.
[29] A. Konnov, Detailed Reaction Mechanism for Small Hydrocarbons Combustion, Release 0.5, 2000, <http://homepages.vub.ac.be/≃akonnov/>.
[30] K. Takashima, Z. Yin, I.V. Adamovich, Plasma Sources Sci. Technol. 22 (2013) 015013.
[31] I.V. Adamovich, M. Nishihara, I. Choi, M. Uddi, W.R. Lempert, Phys. Plasmas 16 (2009) 113505.
[32] J.A. Coxon, Can. J. Phys. 58 (1980) 933–949.
[33] J. Luque, D.R. Crosley, SRI International, Report MP-99-009, 1999.
[34] P.H. Paul, J. Phys. Chem. 99 (1995) 8472–8476.
[35] P. Beaud, P.P. Radi, D. Franzke, H.-M. Frey, B. Mischler, A.-P. Tzannis, T. Gerber, Appl. Opt. 37 (1998) 3354–3367.
[36] D.R. Bates, Planet. Space Sci. 32 (1984) 785–790.
[37] A. Bucholtz, Appl. Opt. 34 (1995) 2765–2773.
[38] Z. Yin, C.D. Carter, W.R. Lempert, I.V. Adamovich, AIAA Paper 2013–0432, in: 51st AIAA Aerospace Sciences Meeting, 7–10 January 2013, Grapevine, Texas.
[39] R.E. Palmer, SAND89-8206, Sandia National Labs., Livermore, CA, 1989.
[40] R. Atkinson, D.L. Baulch, R.A. Cox, J.N. Crowley, R.F. Hampson, R.G. Hynes, M.E. Jenkin, M.J. Rossi, J. Troe, Atmos. Chem. Phys. 4 (2004) 1461–1738.